Bull. Astr. Soc. India (2000) **28**, 515-527

Far-infrared observations of three compact IRAS sources in Sh 247 star forming complex: IRAS 06056+2131, 06058+2138 and 06061+2151

S.K. Ghosh[1], K.V.K. Iyengar[2], A.D. Karnik[1], T.N. Rengarajan[1], S.N. Tandon[3] and R.P. Verma[1]

[1]*Tata Institute of Fundamental Research, Homi Bhabha Road, Mumbai 400005, India*
[2]*285, 17D Main Road, 3rd Block, Rajajinagar, Bangalore 560 010, India*
[3]*Inter-University Centre for Astronomy and Astrophysics, Poona University Campus, Pune 411007, India*

Received 10 November 1999; accepted 23 March 2000

Abstract. Three compact IRAS sources — IRAS 06056+2131, 06058+2138 and 06061+2151 in the Sh 247 complex and having IRAS colours typical of compact H II regions have been observed in the far-infrared using the TIFR 1 m balloon-borne telescope. The observations were done simultaneously in two bands; from these intensity maps at 58 μm and 150 μm with a spatial resolution of 1.′5 have been obtained. We have also obtained intensity maps in the four IRAS bands of 12, 25, 60 and 100 μm using the HIRES routine. Using these and other available observations the spectral energy distributions (SED) for the three sources have been obtained. Radiation transfer modelling has been undertaken to fit the observed SED and infer the nature and distribution of dust in the envelope. In particular, we find that a r^{-2} density distribution is ruled out. The uniform density fits better for two sources while r^{-1} distribution is better for the third. The total luminosities of the sources imply spectral types in the range O9 to B0; however, only two of them have been detected in the radio continuum, that too at a level much lower than that expected. All three are presumably optically thick at 3.6 cm. Molecular observations available in the lines of CO, CS, NH_3 etc. show dense molecular cores as well as outflows associated with all the three sources. IRAS 06056+2131 shows an extended structure with two cores while IRAS 06061+2151 has probably an additional core. The corresponding structures are also seen in the 25 μm map which has higher resolution. While all the three sources are very young and deeply embedded, the absence of radio continuum and non-fragmentation of the cloud suggest that IRAS 06058+2138 is the youngest of the three.

1. Introduction

We have undertaken a programme of mapping star forming regions in the far-infrared (far-IR) using the TIFR 1 m balloon-borne telescope. We have employed a two band photometer which observes the same part of the sky simultaneously in two bands centred around ~ 58 μm and ~ 150 μm to map both warm and cool dust emissions. The simultaneous availability of two bands

enables us to get accurate estimates of dust temperature and optical depth. In this study, we report our observations of the small diameter H II region complex Sh 247 situated towards Gem OB1 and containing three IRAS sources viz., IRAS 06056+2131, 06058+2138 and 06061+2151. All the three sources have IRAS colours typical of compact H II regions. Our aim was to study the nature of these embedded sources and the relationship of far-IR properties to the physical characteristics derived from other observations like radio continuum, molecular line etc. In addition, we are interested in investigating the nature and distribution of dust in the circumstellar envelope by modelling the spectral energy distribution (SED) using radiation transfer calculation.

Besides the observations in the far-IR, these sources have also been studied in various other wavelength bands. Carpenter, Snell & Scholerb (1990, 1995a, 1995b), Carpenter et al. (1993) and Snell et al. (1988) have extensively studied these sources in the molecular lines of ^{12}CO, ^{13}CO and CS, in the radio continuum and in the near-IR (NIR) bands. They find that IRAS 06056+2131 and 06058+2138 are outflow sources while IRAS 06061+2151 does not exhibit an outflow. They also find that all the three sources have associated dense CS cores, some with structures. Schreyer et al. (1996) find cores of NH_3 associated with them. As expected for young star forming regions, H_2O masers (Tofani et al., 1995) and OH masers (Baudry et al., 1993) are seen to be associated with the complex. Carpenter et al. (1990) and Kurtz, Churchwell, & Wood (1994) have observed this region in the radio continuum using the VLA. The former find weak ultra compact (UC) H II regions at 6 cm in the vicinity of IRAS 06056+2131 and 06058+2138. The latter observe, at 3.6 cm, a weak UC H II source close to IRAS 06056+2131 and a cluster of three UC H II sources associated with IRAS 06061+2151. Chini et al. (1986) have observed all the three sources in the 1.3 mm band. Observations in the far-IR at $\lambda > 100$ μm enable us to get a more complete picture of dust emission and to relate this to inferences obtained at other wavelengths.

In Sec. 2, we briefly describe the photometer employed and the observational details. In Sec. 3, we present our intensity maps in the two far-IR bands at a resolution of ~ 1.′5. We have also obtained HIRES maps of this region in the IRAS bands of 12, 25, 60 and 100 μm and compare them with our maps. These results, along with data at other wavelengths are discussed in Sec. 4. In particular, we construct the SED of the sources using the fluxes in our bands, the IRAS bands and the 1.3 mm band. This enables us to get a more accurate determination of the luminosity of the exciting sources. The SEDs are used in conjunction with dust radiation transfer models to infer the optical depth and the density distribution around these sources. Finally, we compare observations at different wavelengths and attempt to infer their inter-relationships and possibly the relative evolutionary stages of the sources. The conclusions are summarised in Sec. 5.

2. Observations

The far-IR observations were conducted using the Tata Institute of Fundamental Research (TIFR) 1 m balloon-borne telescope. The balloon was launched from Hyderabad, India (λ = 17°.45N)on November, 29, 1990. The telescope and observational procedure have been described by Ghosh et al. (1988). Briefly, the telescope is an f/8 Cassegrain system with the secondary chopped at 10 Hz with a throw 3.′8. The field of view was 2.′4 defined by a cold aperture in

the focal plane of the telescope. The telescope is stabilised using three null-servo controlled axes viz., the azimuth, elevation (EL) and cross-elevation (XEL). The rms pointing stability is ~ 0.′3. The two band photometer used for the present observation has been described elsewhere (Bisht, 1991; Verma et al., 1994). The incoming beam was split by a restrahlen filter; the field of view aperture was reimaged on to two Ga doped Ge bolometers cooled by liquid helium (~ 1.8 K) thus simultaneously providing the same sky field in two different bands. The bands were defined by cold filters with half power transmission bands of 45-70 μm and 115-160 μm respectively. The effective wavelengths of the two bands, for an incident gray body spectrum of temperature 40 K and emissivity $\varepsilon \alpha \lambda^{-1}$ were 58.5 μm and 145 μm respectively. Both the effective wavelength and the sensitivity of the bands depend on the transmission and incident spectrum. In Table 1, we give the relative sensitivities (Jy per ADC bit of signal) at fixed wavelengths of 58 μm and 150 μm for different temperatures and two emissivity dependences of $\varepsilon \alpha \lambda^{-1}$ and $\varepsilon \alpha \lambda^{-2}$. The absolute calibrations of the two photometric bands were obtained from observations of Jupiter. The systematic uncertainty in this is about 20%. Jupiter was also used for determining the point spread function (PSF).

The mapping was done by offsetting the telescope with respect to the optical star μ Gem to which the star tracker was locked and using a raster scan mode. The offsets in EL and XEL were effected mechanically using a stepper motor pressing against the star tracker gimbals. The scan was done along the cross-elevation axis at a speed of ~ 0.′7 s^{-1} by imposing a triangular wave error signal to the input of XEL servo. At the end of each scan, the elevation offset was changed by ~ 0.′7 resulting in a raster coverage of ~ 30′ x 24′ in XEL x EL. The telescope aspect was obtained from a combination of error signals of the star tracker and the rate gyros and the mechanical offsets (Ghosh et al. 1988).

Table 1. Relative sensitivities (Jy per ADC bit of signal) of the two band photometer

T (K)	S (58 μm)		S (150 μm)	
	$\varepsilon(\lambda) \alpha \lambda^{-1}$	$\varepsilon(\lambda) \alpha \lambda^{-2}$	$\varepsilon(\lambda) \alpha \lambda^{-1}$	$\varepsilon(\lambda) \alpha \lambda^{-2}$
25	0.91	0.92	1.08	1.08
30	0.98	0.98	1.05	1.09
35	1.00	1.00	1.02	1.07
40	1.00	0.99	1.00	1.00
45	0.99	0.98	0.99	0.98
50	0.96	0.97	0.97	0.96

In the present flight, due to an unexpectedly large launch shock the mechanical housing of the screw which defines the EL offset angle was partly damaged. This resulted in an increased play in the position of the screw, leading to larger uncertainty on the EL offset angle. However, inherent redundancy in the telescope aspect sensors (viz., star tracker & rate gyroscopes)

supplemented by a new aspect reconstruction strategy led to a reliable recovery of aspect information. This involved modelling the gyro drifts over short time scales (single XEL scan duration of ~ 30s) and integrating the corrected gryo signals. This procedure was tested and calibrated using data when the EL offset motion was much larger than the uncertainty introduced by the mechanical play. We also checked that the far-IR PSF for Jupiter and the PSF of stars detected by the focal plane optical photometer during the scan of Sh247 were as per expectations. Overall, the aspect error is somewhat larger than usual, upto ~ 1′.

The detector signals were gridded in XEL x EL co-ordinate system with a pixel size of 18″. This grid was deconvolved using the PSF obtained for Jupiter employing a procedure based on Maximum Entropy Method (MEM) (Ghosh et al., 1988). The FWHM of the deconvolved map of Jupiter gives a resolution of 1.′5. Sh 247 region was mapped in two partly overlapping rasters each repeated with increasing and decreasing EL. Maps were generated independently for both halves of the raster (increasing and decreasing EL) and only those sources, positions of which coincided within 1′ in both maps were taken as genuine. Further, any source near the boundary of the raster box was ignored. For the final deconvolution, all rasters were combined to get a single intensity map for each band.

We have also obtained intensity maps in the four IRAS bands of 12, 25, 60 & 100 μm using the HIRES routine of IPAC[1]. For IRAS 06061+2151, spectral information in the range 7.7 to 22.6 μm is also available from the IRAS Low Resolution Spectra (LRS) Catalog.

3. Results

3.1 Balloon-borne observations

In Figures 1a and 1b, we show the intensity contours for the Sh 247 region at 58 μm and 150 μm respectively. Also shown are the boundaries of the scanned area. The maps have been generated by making the location of peak emission of IRAS 06061+2151 to coincide with the IRAS HIRES position. The maps have a resolution of ~ 1.′5. We clearly observe all the three IRAS sources in both bands. The deviation observed for IRAS 06058+2138 is within the absolute position error of our map.

The integrated signal of each source is determined by assuming a gaussian profile and using the *n2gaussfit* routine of IRAF and a box size of 3′ x 3′. The uncertainty in this is ~ 20-25%. To compute the flux density from the observed signal, a knowledge of the incident spectrum is needed. It is seen from Table 1 that this conversion factor changes by less than 10% for a large change in the spectral shape. We have computed the flux density in our two bands from the temperature implied by the ratio of the signals in the two bands and assuming an emissivity index of 1. These values are shown in Table 2 for the three sources. In the 150 μm map, we find two more fainter sources with no IRAS counterparts. If real, they are cooler than the three IRAS sources. We will not discuss them further in this paper.

[1]IPAC is funded by NASA as part of the IRAS extended mission program under contract to JPL.

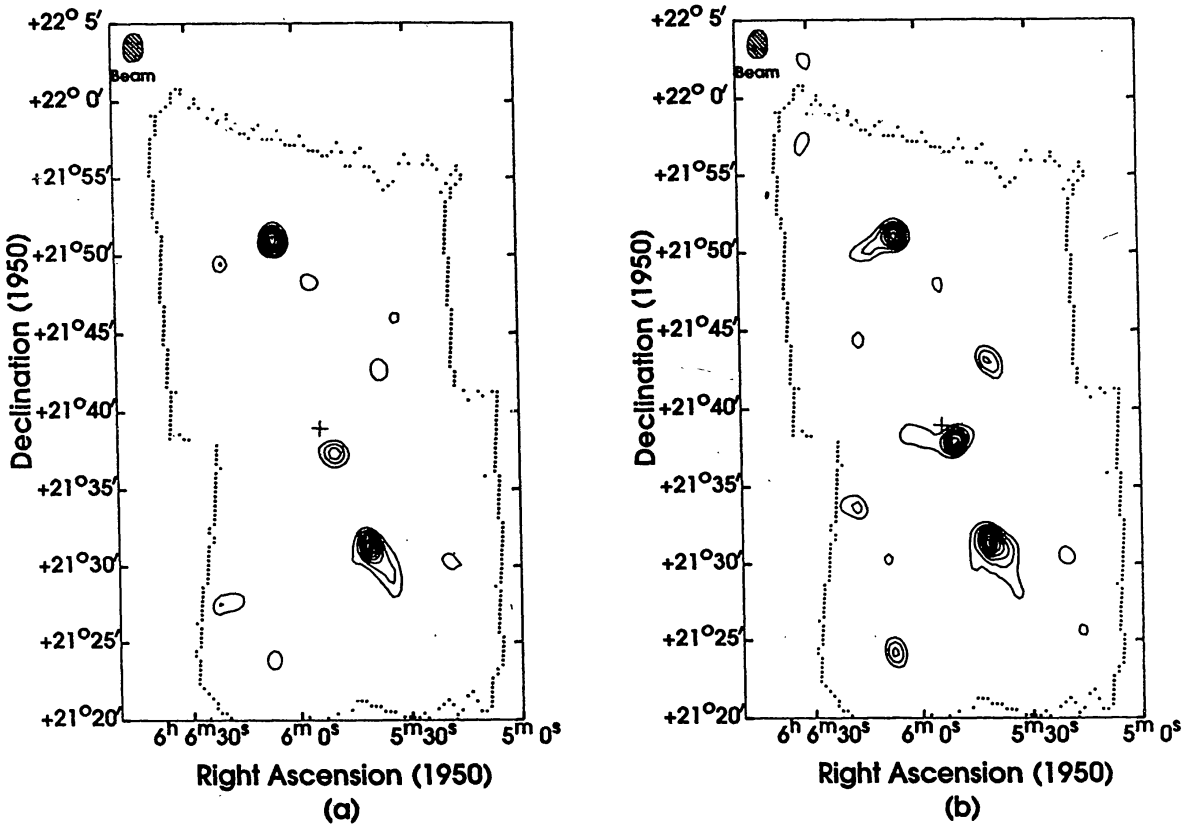

Figure 1. The intensity map of the Sh 247 region. The dashed boundary marks the area scanned. The contour levels are at 0.95, 0.90, 0.80, 0.70, 0.60, 0.50, 0.40, 0.30 and 0.20 of the peak intensity. The (+) symbols are positions from IRAS HIRES maps. a) 58 μm map; peak intensity is 904 Jy arcmin^{-2}. b) 150 μm map; peak intensity is 767 Jy arcmin^{-2}.

3.2 IRAS HIRES maps

In Figures 2a-d, we show the intensity maps at 12, 25, 60 and 100 μm obtained from the IRAS HIRES data. At 60 and 100 μm only the three main sources are seen; however, the higher resolution 12 and 25 μm maps show additional sources and extensions. In our 150 μm map also we find an eastward extension in IRAS 06061+2151 and a NE-SW extension in IRAS 06056+2131 roughly along the same direction as the line joining the two 25 μm sources.

The flux densities in the IRAS bands were also determined using the *n2gaussfit* routine of IRAF. Appropriate colour corrections were applied using the ratios of flux densities in adjacent bands. These and the 1.3 mm flux densities taken from Chini et al. (1986) are also shown in Table 2. For IRAS 06056+2131 and 06058+2138, the IRAS F_{60} extrapolated to 58 μm agrees well with our measurements. For IRAS 06061+2151 the deviation is somewhat larger. We have also computed the total IR luminosity of the three sources assuming a distance of 2.2 kpc following Kömpe et al. (1989) and these are shown in the last row of Table 2.

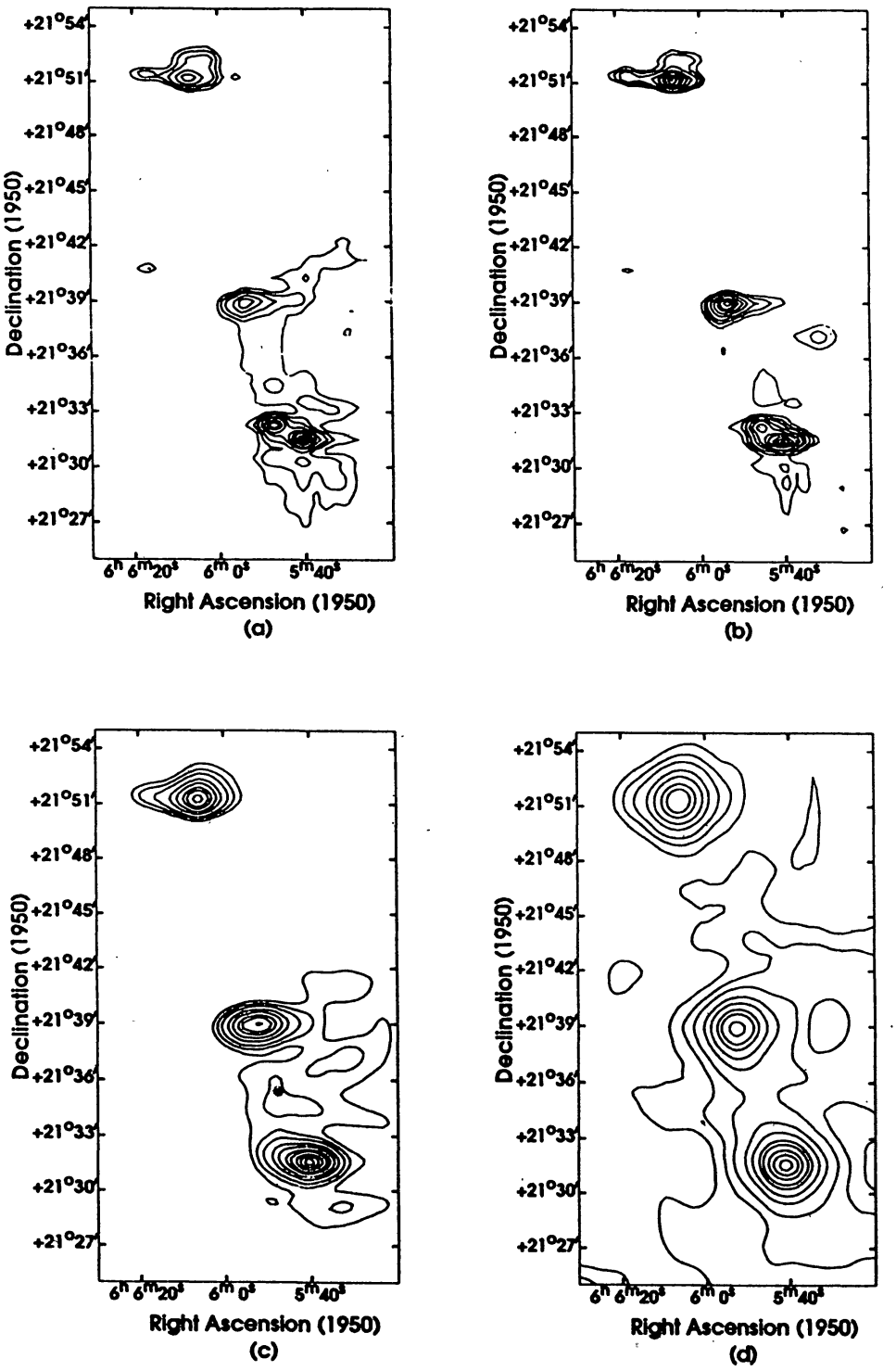

Figure 2. The intensity maps of Sh 247 region derived from the IRAS data using the HIRES routine. The contour levels are at 0.90, 0.70, 0.50, 0.30, 0.20, 0.10, 0.05, 0.02, 0.01 and 0.005 of the peak intensity. a) At 12 μm; the peak intensity is 145 Jy arcmin^{-2}. b) At 25 μm; the peak intensity is 454 Jy arcmin^{-2}. c) At 60 μm; the peak intensity is 1310 Jy arcmin^{-2}. d) At 100 μm; the peak intensity is 828 Jy arcmin^{-2}.

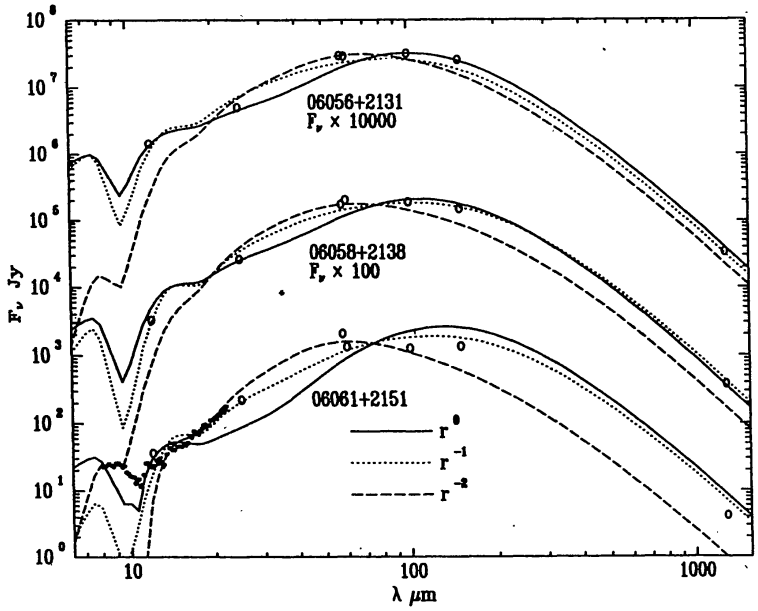

Figure 3. The flux density plotted as a function of wavelength for the three sources in Sh 247 region as given in Table 2. The lines shown are fits from radiation transfer models. Different lines depict fits for three different power law dependence of radial density. Note that, for the sake of clarity flux densities have been multiplied by a different constant factor for two of the sources, for IRAS 06061+2151 LRS data have also been used in the modelling.

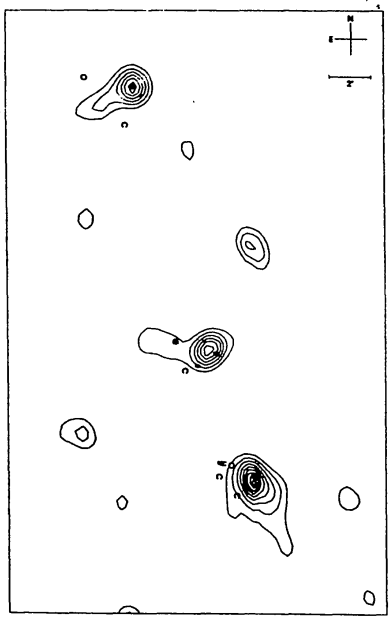

Figure 4. Locations of peaks of radio continuum and molecular line emissions shown superposed on an enlarged 150 μm intensity map of Sh 247 region. The different symbols are: O - faint 25 μm source from IRAS HIRES map; @ - radio continuum at 3.6 cm (Kurtz et al. 1994); # - radio continuum at 6 cm (Carpenter et al. 1990); S - CS emission line (Carpenter et al. 1993, 1995); H - centre of NIR cluster away from the main peak (Carpenter et al. 1993); C - peaks of CO line emission; for IRAS 06056+2131 the peaks of red and blue wings of CO are shown. Note that for IRAS 06061+2151, the peaks of CS and radio continuum emission are very close to the far-IR peak.

Table 2. Spectral energy distribution of sources in Sh 274[a].

Fλ (Jy)	IRAS 06056+2131	IRAS 06058+2138	IRAS 06061+2151
F_{58}	2980.0	1747.0	2071.0
F_{150}	2575.0	1490.0	1352.0
F_{12}	144.6	32.7	36.5
F_{25}	512.2	263.6	223.6
F_{60}	2930.0	2044.0	1326.0
F_{100}	3212.0	1896.0	1266.0
F_{1300}	3.4	3.8	4.2
$L_{IR}/10^4 L_\odot$	3.8	1.9	1.6

[a]The flux densities at 58 and 150 μm are from this work; at 12, 25, 60 and 100 μm are from IRAS HIRES maps and at 1300 μm from Chini et al. (1986). The luminosities given in the last row are from the integration of the SED assuming a distance of 2.2 kpc.

4. Discussion

4.1 Radiative transfer modelling

The photospheric SED of a star deeply embedded in a dust cloud gets modified by the process of dust absorption and re-radiation; the emergent SED is considerably extended to longer wavelengths. The emergent SED depends on the luminosity of the embedded star and the physical conditions of the dust envelope; this can be computed using a radiation transfer model. Here, we use a spherically symmetric model based on the code CSDUST3 (Egan, Leung & Spagna 1988) and a procedure similar to that described by Mookerjea et al. (1999). Only the dust component is used for the model. The main parameters used are the luminosity of the central star, the nature of dust and its emissivity, the density distribution of dust and r_{min} and r_{max}, the inner and outer radii of the dust shell. A mixture of silicate and graphite grains and power law size distribution in accordance with Mathis, Rumpl & Nordsieck (1977) are used; the absorption and scattering efficiencies as a function of wavelength are taken from Draine & Lee (1984) and Laor & Draine (1993). For the density distribution, three different power laws $\rho(r) \propto r^{-n}$ with n = 0, 1 and 2 respectively are employed. The photospheric temperature of the star is taken to be that of a ZAMS star of bolometric luminosity equal to that listed in Table 2. The LRS data of IRAS 06061+2151 show an absorption feature at 10.6 μm. Taking this to be due to SiC (Laor & Draine 1993), we have also incorporated SiC grains while modelling this source. Computations are done keeping n, the density index at a constant value and employing a χ^2 minimisation procedure to find the best fit values for the other parameters. Figure 3 shows the results of the computation for all the three sources for n = 0, 1 and 2. For clarity of presentation, the flux densities have been shifted by 2 and 4 dex for two sources. It is seen

that for all the three sources, the case n = 2 gives a very poor fit. It is also noted that while the best fits for IRAS 06056+2131 and 06061+2151 are obtained for n = 0, the best fit for IRAS 06058+2138 is for n = 1. For IRAS 06056+2131 and 06058+2138, the graphite and silicate grains are needed roughly in equal proportion. In the case of IRAS 06061+2151, we find that the fit for the absorption feature in LRS is better for n = 0 than for n = 1 while the reverse is the case for the ~ 16 - 22 μm continuum. The observed absorption feature is broader than that expected for SiC alone, indicating the need for incorporating silicate grains also which have a broader absorption feature. We investigated this by using only SiC and graphite grains and find that the fit is indeed poor. In summary, our calculations show that the dust density distribution has power law index of 0 – 1. Many other studies have also shown that the far-IR dust envelope most often has a uniform density (Churchwell 1990; Faison et al. 1998; Mookerjea et al. 1999). This is quite different from the value n = 1.5 expected near the collapsing core (Shu, Adams & Lizano 1987). This is probably due to the outer pc size envelope sampled by far-IR emission remaining unaffected and/or due to modification of the density distribution near the core by the outflow and the intense radiation associated with a high mass star.

In Table 3, we present the parameters of the best fit for all the three sources. In the same Table we also give the computed dust masses using the same emissivity as used in the modelling. Also given are the gas masses of the cores from molecular observations (CS: Carpenter et al. 1993; CO: Kömpe et al. 1989). The gas to dust ratios computed from these are also shown in the Table 2. The gas mass computed from CO observations is for a size larger than that for CS and as such may be an overestimate. It is seen that the gas to dust ratio for the three sources is, within errors, about the same as the standard ISM value.

Table 3. Parameters of the best fit radiation transfer model to the SEDs of sources in Sh247.

Parameter	IRAS 06056+2131	IRAS 06058+2138	IRAS 06061+2151
r_{min} (pc)	0.010	0.011	0.004
r_{max} (pc)	0.679	1.030	0.713
Density Index (n)	0	1	0
τ_{100}	0.054	0.10	0.14
f_{sil}	0.6	0.5	0.18
f_{SiC}	-	-	.08
$M_{dust}/M_{\odot}$	13.1	17.9	34.1
$(M_{gas}/M_{\odot})$	3750[a]	3725[a]	6200[b]
M_{gas}/M_{dust}	287	169	182

[a] From CS observation of Carpenter et al. (1993) using a distance of 2.2 kpc

[b] From CO observations of Kömpe et al. (1989)

4.2 Comparison with molecular lines and radio continuum observations

The Sh 247 region has been observed in several lines of molecules like ^{12}CO, ^{13}CO, CS, NH_3, H_2O, OH masers and HCO^+. In general, the locations of the centres of the molecular cores coincide with each other as well as with the far-IR positions. Some of them show extended emission and additional structures. The region has also been mapped in the radio continuum and imaged in the NIR. In order to facilitate comparison of locations of different sources, we show them in Figure 4 superposed on the far-IR map. For molecular lines, only those peaks that differ in position are shown. Also displayed are additional weak sources seen at 25 μm. In the following subsections, we will discuss the three sources individually.

4.2.1. IRAS 06056+2131

Snell et al. (1988) who have observed this source in the CO line find it to be a typical bipolar outflow source wherein the peaks of blue and red wings are spatially separated. The outflow is in the NE-SW direction. Shepherd & Churchwell (1996) have also observed the outflow and find the wing spread to be 34.4 km s^{-1}. Ammonia line observation of Schreyer et al. (1996) shows a peak centred on the IRAS position, but extended in the NE-SW direction. CS observation of Carpenter et al. (1993) also shows an extension in the same direction; further they find a secondary peak NW of the main source. Morata et al. (1997) also find two CS cores as well as an extension in the direction joining the two sources. IRAS 25 μm intensity map shows a faint source close to the second CS core. Our 150 μm map also shows an extension SW of the main source in about the same direction as the CS, ammonia extension, but we do not observe the NW peak. The NIR imaging of Carpenter et al. (1993) reveals two clusters of star formation coinciding with the main and secondary CS peaks. Thus, it is seen that the morphology traced at different wavelengths is similar. The star formation associated with the north-east CS core is either independent of the main source or, probably, the result of fragmentation due to the formation of the high mass star and induced star formation in the new fragment. There does not seem to be any high mass star associated with this.

Radio continuum observations using the VLA reveal a weak source at 3.6 cm with a flux density of 0.7 mJy (Kurtz et al. 1994) while Carpenter et al. (1990) find a 6 cm flux density of 1.6 mJy associated with the far-IR source. For a single embedded source of bolometric luminosity equal to the far-IR luminosity the expected radio continuum flux density is 1240 mJy.

4.2.2 IRAS 06058+2138

This source has a compact structure at all wavelengths. This is also an outflow source with a wing width of 12-15 km s^{-1} (Snell et al. 1988; Shepherd & Churchwell 1996). Molecular line observations show the presence of only a single core (CS: Carpenter et al. 1993; NH_3: Schreyer et al. 1996). Polarimetric observations in the NIR by Tamura et al. (1991) reveal a centre-symmetric structure. In the radio continuum, Carpenter et al. (1990) report a 6 cm source of flux density 2 mJy, offset by 25″. On the other hand, Kurtz et al. (1994) and Tofani et al. (1995) do not find any radio continuum source. The former find a source about 95″ away. If the embedded source were optically thin, the expected 3.6 cm continuum is 171 mJy.

NIR imaging observations of Carpenter et al. (1993) reveal only a single cluster of stars centred on the molecular core. The brightest star in the cluster has saturated signal corresponding to a H magnitude of 8. If we derive the extinction by extrapolating the τ_{100} given in Table 3, we get an extinction correction of $A_H = 7.2$; using a distance of 2.2 kpc, this translates to an absolute magnitude of $M_H \leq -10.9$. The star could be fainter if it is located not in the centre of the cloud, but towards the front. The corrected magnitude can be compared with the absolute magnitude $M_H = -3.3$, expected if it is a ZAMS and is the source of the far-IR radiation. Since, the corrected H magnitude is much lower than this value, it is clear that it cannot be a main sequence star. Most likely, it is a Herbig Be star with a high NIR excess. It may be noted that Hillenbrand et al. (1992) find NIR excess of 2-3 magnitudes for a sample of Herbig Ae-Be stars. Carpenter et al. (1993) have also pointed out this; they are of the opinion that most of the bright stars in clusters observed by them are such stars.

4.2.3 IRAS 06061+2151

Schreyer et al. (1996) observe an ammonia cloud associated with this source. They also find an extension to the east, with an indication that there may be a second peak. It is interesting to note that IRAS map also shows a faint 25 μm source east of the main source. Our 150 μm map also shows an eastern extension. Snell et al. (1988) who observed it in the ^{12}CO line do not find an outflow associated with this source. However, Shepherd & Churchwell (1996) observe a CO velocity wing width of 28.4 km s^{-1}, characteristic of an outflow source. Carpenter et al. (1995b) find only a single CS core. Kurtz et al. (1994) observed this region with the VLA in the 3.6 cm radio continuum and find a cluster of three sources, closely spaced (within ~ 10″) and coinciding with the IRAS position. The total flux density at 3.6 cm is only 4.6 mJy, much less than the value of 96 mJy expected if it were a single ZAMS star of bolometric luminosity equal to the far-IR luminosity. This is again consistent with these being optically thick UC HII sources. There is no NIR observation for this source.

4.3 Optical depth in the radio continuum

We find that the observed radio continuum emission from all the three sources is much less than that expected for an optically thin case. If this discrepancy is attributed to optical depth effect, the observed $\tau_{3.6}$ for IRAS 06056+2131, 06058+2138 and 06061+2151 are 7.5, > 5.1 (assuming an upper limit of 1 mJy) and 3.0 respectively. We then compute the corresponding emission measure, E to be 1.5×10^8, $> 1.02 \times 10^8$ and 6×10^7 pc cm^{-6} respectively. We can also compute the emission measure from the model fits discussed in section 4.1. Taking the case of uniform density as an example and assuming that an approximate measure of E is 150 $\rho_d r_{min}/m_H$ (for gas to dust ratio of 150 by mass), the values are found to be 3.7×10^7, 5.7×10^7 and 1.88×10^8 pc cm^{-6}. These values are close to the values computed earlier. Thus we conclude that the discrepancy of radio continuum emission observed is due to optical depth effects.

4.4 Evolutionary status

All the three sources are deeply embedded OB stars exhibiting several characteristics of very young stars. Can one say anything about the relative evolutionary stages of these sources? With the passage of time, the environment of OB stars is affected by the effects of high stellar

radiation and outflows which may lead to elongation of the cloud structure and later fragmentation of the parent cloud. IRAS 06056+2131 and 06061+2151 show such structures. In the latter, Kurtz et al. (1994) found three weak radio continuum sources. However, IRAS 06058+2138 does not have associated radio continuum and shows a single compact structure at all wavelengths. Hence this appears to be the youngest of the three sources.

5. Conclusion

We have observed the Sh 247 star forming complex containing three IRAS sources - IRAS 06056+2131, 06058+2138 and 06061+2151 in the far-IR using the TIFR 1 m balloon-borne telescope and have obtained ~ 1.′5 resolution intensity maps simultaneously in two bands centred on 58 μm and 150 μm. We have also obtained IRAS HIRES maps in the four IRAS bands. There are indications of some extension in the 150 μm contours in the case of IRAS 06056+2131 and 06061+2151 roughly in alignment with directions of outflows mapped in molecular lines. The IRAS HIRES map at 25 μm also shows additional sources along the same directions. Using our data, the IRAS data and 1.3 mm observations, we construct the SED for the three sources. From this we obtain, assuming a distance of 2.2 kpc, a luminosity of (3.8, 1.9 and 1.6) x 10^4 $L_\odot$ for IRAS 06056+2131, 06058+2138 and 06061+2151 respectively. The corresponding ZAMS spectral types are O9.5, B0-B0.5 and B0-B0.5.

We investigate the physical condition of the dust envelope using radiation transfer model to best fit the observed SED and thus obtain the values of inner and outer radii of the envelope, the dust optical depth at 100 μm and hence the dust mass for three different radial density profiles viz., uniform, r^{-1} and r^{-2}. We find that the r^{-2} density profile can be ruled out for all three sources. Using the dust masses derived and the gas mass obtained for associated molecular clouds, the gas to dust mass ratio is found to be in the same range as for the Milky Way ISM.

The deficiency of observed radio continuum emission as compared to the expectation for optically thin case indicates optical depths of 3-7. The emission measures derived from these optical depths and from modelling are in agreement.

All three sources have associated molecular cores as revealed by CO, CS and NH_3 molecular line observations. In the case of IRAS 06061+2151 and 06056+2131, the gas is extended with additional cores; the far-IR emissions also roughly trace these. This fragmentation is probably due to the effects of outflows of gas and radiation affecting the cloud structure. IRAS 06058+2138 does not seem to have an associated UC H II region. The gas is also concentrated in a single compact core. These indicate that IRAS 06058+2138 is at an earlier stage of evolution as compared to the other two sources.

We thank the members of the TIFR National Balloon Facility, Hyderabad and the Balloon Support Instrumentation Group for providing support for the balloon flight. We thank S.L.A. D'Costa, G.S. Meshram, M.V. Naik and D.M. Patkar for valuable technical support for the program. We thank B. Das, S.L.A. D'Costa and H.T. Saraiya for their help during the balloon flight as well as in the data analysis.

References

Baudry A., Menten K.N., Walmsley C.M., Wilson T.L., 1993, A&A, 271, 552

Bisht R.S., 1991, Ph. D. Thesis, Bombay University

Carpenter J.M., Snell R.L., Schloerb F.P., 1990, ApJ, 362, 147

Carpenter J.M., Snell R.L., Schloerb F.P., 1995a, ApJ, 445, 246

Carpenter J.M., Snell R.L., Schloerb F.P., 1995b, ApJ, 450, 201

Carpenter J.M., Snell R.L., Schloerb F.P., Skrutskie M.F., 1993, ApJ, 407, 657

Chini R., Kreysa E., Mezger P.G., Gemünd H.P., 1986, A&A, 154, L8

Churchwell E., 1990, in Lada C.J., Kylafis N.D., eds The NATO ASI Services, The Physics of Star Formation and Early Stellar Evolution, Kluwer Dordrecht, p 221

Draine B.T., Lee H.M., 1984, ApJ, 285, 89

Egan M.P., Leung C.M., Spagna G.F., Computer Physics Communications, 1988, 48, 271

Faison M., Churchwell E., Hofner P., Hackwell J., Lynch D.K., Russel R.W., ApJ, 1998, 500, 280

Ghosh S.K., Iyengar K.V.K., Rengarajan T.N., TAndon S.N., Verma R.P., Daniel R. R., 1988, ApJ, 330, 928

Hillenbrand L.A., Strom S.E., Vrba F.J., Keene J., 1992, ApJ, 397, 613

Kömpe C., Joncas G. Baudry A., Wouterloot J.G.A., 1989, A&A, 221, 295

Kurtz S., Churchwell E., Wood D.O.S., 1994, ApJS, 91, 659

Laor A., Draine B.T., 1993, ApJ, 402, 441

Mathis J.S., Rumpl W., Nordsieck K.H. 1977, ApJ, 217, 425

Morata O., Estalella R., Lopez R., Planesas P., 1997, M.N.R.A.S., 292, 120

Mookerjea B., Ghosh S.K., Karnik A.D., Rengarajan T.N., Tandon S.N., Verma R.P., 1999, ApJ, 522, 285

Schreyer K., Henning Th., Kömpe C., Harjunpää P., 1996, A&A, 306, 267

Shepherd D.S., Churchwell E., 1996, ApJ, 457, 267

Shu F.H., Adams F.C., Lizano S., 1987, ARA&A, 25, 23

Snell R.L., Huang Y.L., Dickman R.L., Claussen, M.J., 1988, ApJ, 325, 853

Tamura M., Gatley I., Joyce R.R., Ueno M., Suto H., Sekiguchi M., 1991, ApJ, 378, 611

Tofani G., Felli M., Taylor G.B., Hunter T.R, 1995, A&AS, 112, 299

Verma R.P, Bisht R.S., Ghosh S.K., Iyengar K.V.K., Rengarajan T.N., Tandon S.N., 1994, A&A, 284, 936